Journal of Structural Geology 32 (2010) 803–817

Contents lists available at ScienceDirect

Journal of Structural Geology

journal homepage: www.elsevier.com/locate/jsg

Evaluating quartz crystallographic preferred orientations and the role of deformation partitioning using EBSD and fabric analyser techniques

Mark Peternell [a,*], Pavlína Hasalová [b], Christopher J.L. Wilson [a], Sandra Piazolo [c,1], Karel Schulmann [d]

[a] School of Earth Sciences, The University of Melbourne, Victoria 3010, Australia
[b] School of Geosciences, Monash University, Clayton, Victoria 3800, Australia
[c] Department of Geological Sciences, Stockholm University, Stockholm 10691, Sweden
[d] L'Université de Strasbourg, l'Institut de Physique du Globe de Strasbourg, UMR 7517, 1 Rue Blessig, Strasbourg 67084, France

ARTICLE INFO

Article history:
Received 31 October 2009
Received in revised form
5 May 2010
Accepted 13 May 2010
Available online 21 May 2010

Keywords:
Crystallographic preferred orientation
Deformation partitioning
Electron back-scattered diffraction
Fabric analyser
Quartz
Thaya dome

ABSTRACT

Quartz crystallographic preferred orientations (CPO) from three distinct orthogneisses using both the Electron Back Scatter Diffraction (EBSD) and Fabric Analyser (FA) techniques reveal a clear trend from basal <a> and rhomb <a + c> slip for high P–T conditions (670 ± 20 °C/9 kbar), rhomb <a + c> and basal <a> slip for medium P–T (590 ± 15 °C/6 kbar) and a dominance of prism <a> slip for lower P–T conditions (<570 °C/4–5 kbar). The textural variations are interpreted in terms of a temperature field gradient and microscale strain partitioning controlled by a weak feldspar matrix that can locally invert the expected slip system sequences. Locally quartz CPOs are different within one thin section, and in comparison to bulk orientation measurements both, EBSD and the Fabric Analyser techniques are ideal to determine such textural heterogeneities. While the EBSD is a powerful technique to determine the full CPO, measurements from similar locations inside several quartz grains from the orthogneisses and an annealed and undeformed quartzite show that the FA is an accurate tool to determine CPOs of *c*-axis orientations in uniaxial materials. In a CPO focussed study the FA is a cheap alternative to EBSD as the analysis of whole thin section can be accomplished in a very short time, with minimal sample preparation. With the FA it is possible to evaluate the CPOs of several samples quickly with an accuracy that allows identification of the main slip systems and their homogeneity.

© 2010 Elsevier Ltd. All rights reserved.

1. Introduction

Crystallographic Preferred Orientation (CPO) measurement in deformed rocks is a common procedure introduced into classical structural analysis (e.g. Sander, 1930; Fairbairn, 1949; Turner and Weiss, 1963). A CPO analysis is crucial in order to decipher observed microstructures and/or deformation mechanisms (e.g. Prior and Wheeler, 1999), model other physical anisotropies of rocks (e.g. Ji and Mainprice, 1988; Bascou et al., 2001) and to understand and quantify sedimentary, metamorphic and magmatic processes (e.g. Mørk and Moen, 2007; Romeo et al., 2007; Hasalová et al., 2008).

Quartz is one of the most common minerals in the Earth's crust and therefore understanding its deformational behaviour is important. There are many studies of experimentally and naturally deformed quartz-rich rocks that provide some insight in understanding of quartz deformational behaviour and development of its CPO (Hobbs, 1968; Tullis, 1977; Blumenfeld et al., 1986; Schmid and Casey, 1986; Dell'Angelo and Tullis, 1989; Gleason et al., 1993; Stipp et al., 2002; Vernooij et al., 2006; Menegon et al., 2008; Stipp and Kunze, 2008). Quartz CPO is controlled by temperature, strain rate, differential stress and fluid content (e.g. Stipp et al., 2002; Menegon et al., 2008). Therefore deformed quartz has distinctive CPOs that can be related to specific conditions of formation (e.g. Tullis, 1977; Schmid and Casey, 1986; Stipp et al., 2002).

A CPO can be obtained either by single grain measurements or by statistical diffraction experiments (volume texture measurements). The latter includes methods such as X-ray diffraction or neutron diffraction (Wenk et al., 1984, 1986). Single grain measurements are based on the determination of the orientation of selected lattice directions, or the complete orientation of individual crystals in a sample (Ullemeyer et al., 2000). The Electron Back Scatter Diffraction (EBSD) method adapted to a Scanning Electron Microscope (e.g. Lloyd et al., 1991; Adams et al., 1993; Prior et al., 1999) is a commonly used method. Other methods are based on optical microscopy using the universal stage (Berek, 1924;

* Corresponding author. Tel.: +61 3 8344 6910; fax: +61 3 8344 7761.
E-mail address: petm@unimelb.edu.au (M. Peternell).
[1] Present address: Department of Earth and Planetary Sciences, Macquarie University, Australia.

0191-8141/$ – see front matter © 2010 Elsevier Ltd. All rights reserved.
doi:10.1016/j.jsg.2010.05.007

Reinhard, 1931; Turner and Weiss, 1963) or computer assisted microscope stages (Heilbronner and Pauli, 1993; Fueten, 1997; Fueten and Goodchild, 2001; Wilson et al., 2003, 2007). All of these methods have specific advantages and restrictions. The choice of technique depends on the problem being investigated, e.g. which minerals are measured, grain size, whether a thin section or hand specimen is analysed, if the rock is mono- or polymineralic and if it is important to link crystallographic orientations to the exact microstructural position.

The EBSD method provides the easiest way of acquiring large numbers of complete CPO data from individual rock forming minerals with a spatial resolution of <1 μm with a simultaneous knowledge of the microstructure. As in a Scanning Electron Microscope the electron beam creates a source of scattered electrons within a specimen, diffraction of these electrons will occur simultaneously on all lattice planes in a polygrained sample and the back-scattered electrons will form a diffraction pattern and provide the orientation of individual grains (for details see Prior et al., 1999). The newest 'High-speed EBSD' technique can acquire more than 1000 images per second, while the mineral indexing is performed offline (Schwarzer and Hjelen, 2010). Nevertheless, 'High-speed EBSD' can only be applied on suitable materials such as aluminium or nickel and therefore, is not usable for rock and mineral samples (Schwarzer and Hjelen, 2010). The speed of automatic EBSD data collection for minerals including quartz is less than 20 points per second (Prior, 2009).

In summary, advantages of the EBSD method are its high spatial and angular resolution, automatic recognition of mineral phases and that the complete crystallographic orientation including all crystallographic axes, i.e. including Dauphiné twins, can be determined. On the other hand, some extra sample preparation is needed and even with directed automatic EBSD data acquisition the analysis of larger areas, i.e. whole thin section will in general take longer and therefore makes this technique in comparison to the fabric analysis technique described in this paper more expensive.

As an alternative, the optical technique such as the FA (Wilson et al., 2003, 2007) is a fast and a sufficiently accurate tool to determine individual *c*-axis orientation of uniaxial minerals such a quartz, calcite or apatite. Samples can be analysed with a resolution of ~2.8μm/pixel and no special sample preparation is needed. Covered, uncovered, polished, coated or stained thin sections as well as mounts for fission track analysis can be analysed (Peternell et al., 2009). The biggest advantages of the FA are its ability to measure up to 10 × 10 cm sized samples and its speed and ease of operation. With the standard setting used in this study approximately 90 000 pixels per second can be acquired. Nevertheless, because of the used 2 Ghz desktop computer for image processing, the real-time analysis for a whole thin section (~4 × 2.5 cm) is slowed down to <45 min with 50 μm/pixel, <2 h with 5 μm/pixel and <8 h with 2.8 μm/pixel resolution. The result of the analysis is presented as an axial-distribution (AVA) image of the *c*-axis orientation for each pixel (Heilbronner and Pauli, 1993; Fueten, 1997; Fueten and Goodchild, 2001; Wilson et al., 2003, 2007, 2009). Disadvantages of the method are its limitation to analyse not the full crystallographic orientation, its current restriction to hexagonal and trigonal minerals, and lower spatial and angular resolution in comparison to the EBSD. In summary, FA and EBSD are very valuable alternatives for specific questions as the type of data and sample preparations are different.

The aim of this work is (i) to evaluate the accuracy of quartz CPO data obtained from the FA by comparing results to EBSD analysis (using both the HKL and the TSL systems) and (ii) to discuss the role of deformation partitioning in the development of quartz CPOs.

Wilson et al. (2007) conducted on one sample a first comparison between CPO data obtained by EBSD and FA. However, this was done using an earlier version of the FA and no single point comparison, crystal mapping or *c*-axis distribution within a single thin section was performed. In this study we perform a more rigorous evaluation of the accuracy of FA data by analysing an undeformed Appin Quartzite from the Ballachulish contact aureole, Scotland and a deformed medium-high grade orthogneisses from the Thaya dome in the Bohemian Massif (Czech Republic). The quartz CPOs were measured in four different ways: (i) Single crystal orientation maps, (ii) point orientations within individual quartz crystals, (iii) bulk *c*-axis orientations and (iv) distribution of *c*-axes orientations on the thin section scale. Advantages and disadvantages of both techniques will be discussed in detail, as well as the problem of texture heterogeneity determination on a thin section scale.

Results show that Thaya samples show different quartz CPOs as a result of different deformation and metamorphic conditions. The peak P–T conditions change from c. 670 ± 20 °C/9 kbar to 570 °C/4–5 kbar. Quartz *c*-axis orientations in the distinct orthogneiss samples will be discussed in relation to deformation and metamorphic conditions they underwent. Finally, results will be linked to their implication for microstructural development on the regional scale.

2. Geological setting of the Thaya Dome

The Thaya Dome (or so-called Thaya tectonic window) is situated at the southeast margin of the Bohemian Massif (Fig. 1a) and consists of par-autochtonous Brunia basement (Dudek, 1980) and two basement derived nappes – Lower Moravian Nappe (LMN) and Upper Moravian Nappe (UMN; Fig. 1b) (Schulmann et al., 1995). The basement consists of the Cadomian Thaya granite/orthogneiss overlain by a Proterozoic metapelitic and metapsamitic sequence. The lower Moravian Nappe consists of the strongly sheared Weitersfeld orthogneiss at the base that is overlain by metapelites, marbles and calc-silicate rocks. The Upper Moravian Nappe is composed of the Bíteš orthogneiss body at the base and a metavolcano-sedimentary cover in the upper part of the section (Fig. 1b) (Schulmann, 1990; Schulmann et al., 1994).

The Thaya Dome reveals inverted Barrovian metamorphism interpreted as a result of continental underthrusting and later imbrications of crustal nappes (Štípská and Schulmann, 1995). The structurally highest unit in the western part (Upper Moravian Nappe) exhibits the highest grade of metamorphism (Suess, 1912). Peak metamorphic conditions for these three orthogneiss units were estimated from interlayered metapelites by average P–T method and standard Grt–Bt, St–Grt and Grt–Plg thermobarometry and are ranging from ~650 °C/10 kbar to ~500 °C/4 kbar (Štípská and Schulmann, 1995; Štípská et al., 2000). The kyanite-sillimanite bearing metapelites adjacent and interlayered with the Bíteš orthogneiss reveal metamorphic peak conditions of ~670 ± 20 °C at 9 kbar. Staurolite bearing metapelites spatially connected with the Weitersfeld orthogneiss show peak metamorphic conditions ~590 ± 15 °C at 6 kbar and the garnet bearing metasediments overlying the Thaya orthogneiss at the western border of the Brunia basement exhibit the lowest peak metamorphic conditions below 570 °C at 4–5 kbar (Štípská and Schulmann, 1995). Consequently, the peak metamorphic conditions of these three orthogneisses and associated metasediments match different crustal levels from where they were exhumed and therefore influence the mineral textures and microstructures of these rocks (Ulrich et al., 2002). In conclusion, the Upper Moravian Nappe was hotter than the Lower Moravian Nappe and the Brunia basement and these differences have led to temperature dependent variations in active slip systems of quartz and therefore also in analysed textures. The Bíteš, Weitersfeld and Thaya orthogneisses

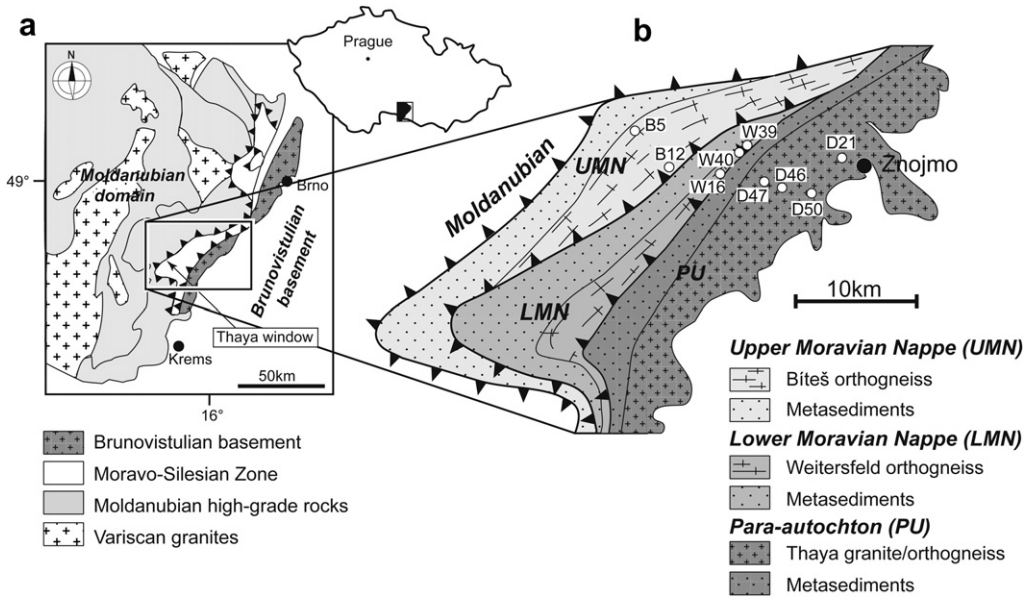

Fig. 1. (a) Simplified geological map of the eastern margin of the Bohemian Massif with main tectonic units and major thrust indicated. The upper right inset shows the general location of the studied area within the Czech Republic. (b) Detail map showing the major unit of the Thaya Dome (modified after Štípská et al., 2000). Locations of studied samples are indicated.

reveal textural variations that are interpreted as a result of inverted metamorphic field gradient described above.

3. Sample description

3.1. The Thaya orthogneisses

To cover different microstructural variations we have analysed 9 deformed orthogneiss samples from the Thaya Dome – 2 from the Bíteš orthogneiss (B5, B12), 3 from the Weitersfeld orthogneiss (W16, W39a, W40) and 4 from the Thaya orthogneiss (D50a, D47a, D46b, D21a). The textures were studied in thin sections cut perpendicular to foliation and parallel to lineation (XZ section), thin sections were carbon coated and in order to distinguish between feldspars some samples were stained (using the method of Bailey and Stevens, 1960). The orthogneisses consist mainly of quartz, K-feldspar, plagioclase, biotite and muscovite. Garnet is present in some samples of the Bíteš orthogneiss; epidote and chlorite growing at the expense of biotite are present in some samples of the Thaya orthogneiss. The three studied orthogneisses show a variety of microstructures resulting from different peak metamorphic conditions and related deformation (Fig. 2).

The Bíteš orthogneiss (Fig. 2a) is a medium to coarse grained high grade orthogneiss. The orthogneiss reveals a well-developed foliation defined by large recrystallised feldspar and quartz aggregates (Fig. 2a). Quartz forms wide (up to 0.5 mm) strongly elongated ribbons defining a stretching lineation. Both, quartz (0.3–1.5 mm in size) and feldspars (0.2–0.4 mm in size) grains show lobate boundaries suggesting grain boundary migration recrystallisation mechanism (Fig. 2b). Quartz commonly exhibits wavy extinction and subgrain formation (Fig. 2b).

The Weitersfeld orthogneiss (Fig. 2c) is dominated by recrystallised plagioclase alternating with irregularly distributed elongated quartz aggregates/ribbons and layers of relics K-feldspar porphyroclasts (Fig. 2c). Quartz (0.3–0.8 mm in size) is either irregularly distributed as aggregates or forms highly elongated ribbons (Fig. 2c). Both feldspars show a polygonal texture with straight boundaries meeting in triple point junctions (Fig. 2d), indicating grain boundary reorganisation by surface energy reduction related to deformation.

The Thaya Orthogneiss (Fig. 2e) represents the lowest metamorphic grade and consists of a fine grained matrix of recrystallised plagioclase and elongated aggregates of quartz containing relics of large K-feldspar and plagioclase porphyroclasts (Fig. 2e). Quartz (0.1–0.4 mm in size) has lobate boundaries and forms elongated polycrystalline aggregates (Fig. 2e,f). Low temperature features as undulose extinction, prismatic subgrain boundaries at high angle to ribbon boundaries are present. Quartz, plagioclase and K-feldspar show core and mantle microstructures suggesting subgrain rotation recrystallisation (Fig. 2f).

3.2. The Appin quartzite

The Appin quartzite is part of a well-developed contact aureole of the Ballachulish intrusive complex in the Scottish Highlands. The P–T conditions in the aureole range from ~480 °C up to 700–800 °C (e.g. Pattison and Harte, 1997). However, the Appin quartzite shows extensive melting only in a narrow region close to the intrusion. The quartzite comprises ~85 vol% quartz and 15 vol% feldspar (Buntebarth and Voll, 1991). Quartz in the Appin quartzite used in this study (sample 35A, courtesy of H. Bergman) is typically coarse grained (≤1.5 mm), undeformed and statically recrystallised forming a foam-like polygonal texture (Fig. 4a). The sample used for this study has been SYTON®-polished (Fynn and Powell, 1979).

4. Methodology

4.1. Electron back-scattered diffraction

Using EBSD complete crystallographic orientation data of quartz were obtained. All details of instruments used, measurement conditions and sample preparations are summarized in Table 1. While EBSD analyses can be collected automatically by performing a regular grid of measurements, this automatic mapping was rejected due to large grain size of the quartz (~0.2–1.5 mm). Moreover, manual data collection allows interactive indexing and

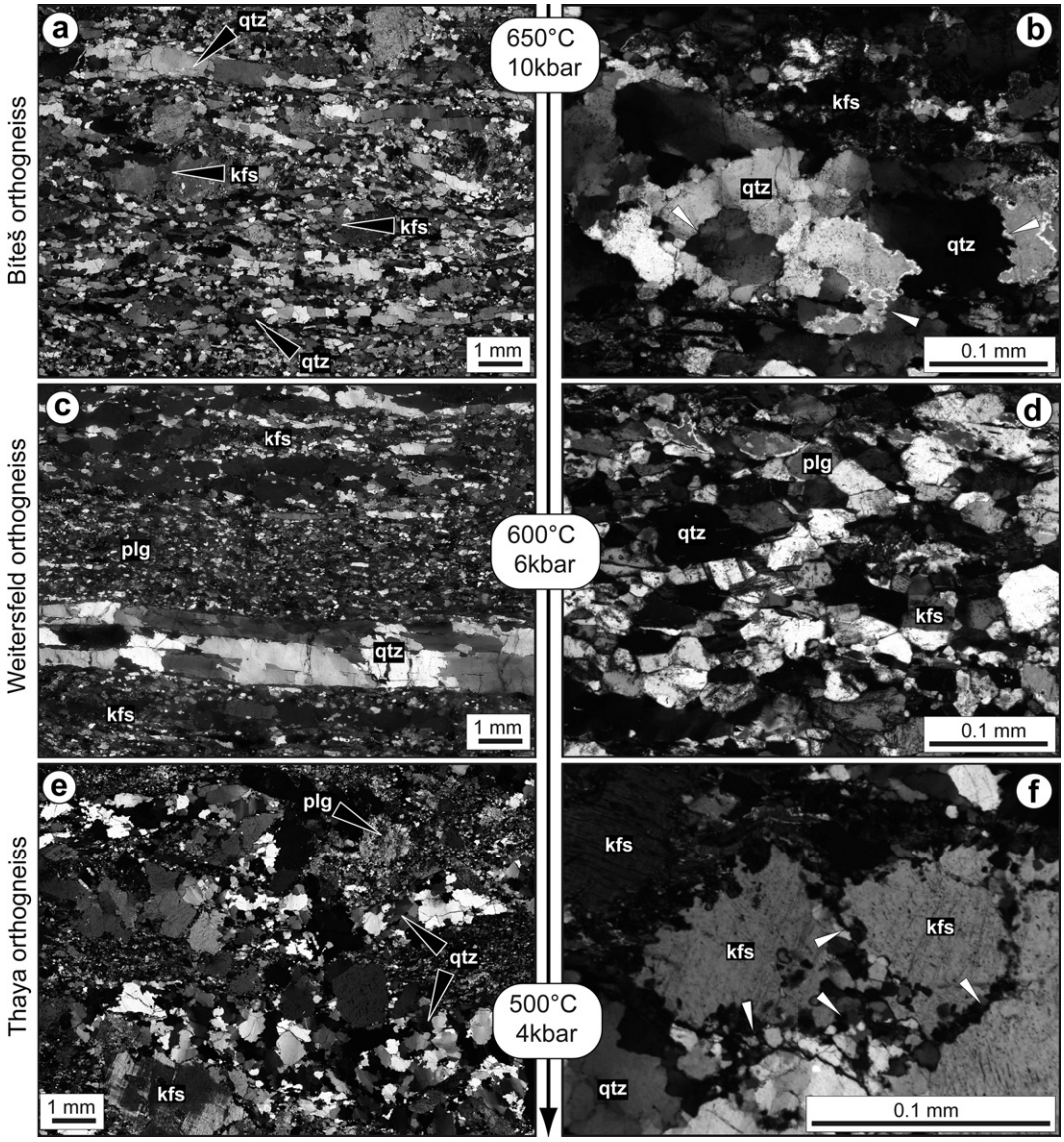

Fig. 2. Photomicrographs showing characteristic microstructures of the three orthogneisses, with emphasis on quartz. (a) High-temperature Bíteš orthogneiss (sample B05) with recrystallised feldspars and quartz forming strongly elongated aggregates. (b) Detail of recrystallised quartz aggregate in Bíteš orthogneiss (sample B12). Quartz display wavy extinction, subgrain formation and highly lobate boundaries (white arrows) indicating grain boundary migration recrystallisation. (c) Banded quartz-feldspar mylonitic Weitersfeld orthogneiss (sample W16) with long quartz ribbons and recrystallised plagioclase alternating with layers of relic K-feldspar porphyroblasts; K-feldspar is stained. (d) Detail of Weitersfeld orthogneiss (sample W16). Quartz, plagioclase and K-feldspar show polygonal texture with straight boundaries meeting in triple point junctions. (e) Porphyritic Thaya orthogneiss (sample D46b) with relics of K-feldspar and plagioclase grains. The fine-grained matrix mainly consists of recrystallised plagioclase and elongated aggregates of recrystallised quartz. (f) K-feldspar in Thaya orthogneiss (sample D46b) showing core and mantle microstructures suggesting subgrain boundary rotation recrystallisation (white arrows).

enables the results from the EBSD to be used as a good standard for later comparison with the FA. To allow a comparison of both methods based on automatic EBSD analysis, whole thin sections would have been mapped by EBSD at 5 μm resolution. This was not done because of long EBSD measuring times on the instrument used (~500 h for a whole thin section at 5 μm resolution). Anyway, we want to emphasise that in general for coarser grained material as used in this study a different setup for EBSD (lower resolution and smart sampling strategy) would allow automated whole thin section bulk CPO analysis with comparable measurement times to the FA. Each individual grain is represented by only one orientation measurement. The resulting pole figures are presented as lower hemisphere equal-area projections in which the trace of foliation is oriented along the equator and the stretching lineation is in the E–W direction.

The spatial resolution of the EBSD used for the Thaya orthogneisses is 6.4 μm/pixel. All EBSD measurements for the Thaya samples are performed manually with <1° accuracy. Therefore, all differences in *c*-axis orientations between EBSD and the FA related to these samples are outside the error that can be assigned to the EBSD technique. For the Appin quartzite crystallographic orientation data were obtained automatically on rectangular grids by moving the electron beam at a regular step size of 5 μm.

4.2. Fabric Analyser

c-axis orientations are determined by the use of an FA G50 at the Melbourne University (Australia) and methods described by Wilson et al. (2003, 2007) and Peternell et al. (2009) and shown in Fig. 3. The analysis of a sample is divided into two stages, the data

Table 1
Table summarizing measurement conditions, details of used instruments and sample preparation.

Instrument; EBSD system	Location	Working conditions	Vacuum	Software	Sample specification	Sample
TESCAN Vega LMU, TSL	ULP Strasbourg (France)	AV = 30 kV WD = 33 mm	high-vacuum mode	TSL OIM 5.1	polished carbon-coated	B12, B5, W39
CamScan 3200; HKL	CGS, Prague (Czech Republic)	AV = 20 kV WD = 33 mm	high-vacuum mode	Oxford Instruments HKL Channel 5.0	polished carbon-coated	W16 W40 D47a D21b D46b D50a
Philips XL-30-ESEM-FEG, HKL	Stockholm University (Sweden)	AV = 25 kV WD = 20 mm BC = 0.8 nA	low-vacuum mode	HKL Channel 5.8	SYTON®-polished uncoated	Appin Quartzite

AV = Accelerating voltage; WD = Working distance; BC = beam current.

acquisition (Fig. 3a) and the data investigation (Fig. 3b). Based on a stack of microphotographs the axial distribution AVA image (Sander, 1950) is generated with a spatial resolution of 5 μm/pixel (Fig. 3a) for the Thaya samples and 2.8 μm/pixel for the annealed Appin quartzite. The *c*-axis orientations of each pixel inside the AVA image are then evaluated using the INVESTIGATOR software (http://www.earthsci.unimelb.edu.au/facilities/analyser/downloads.html; Fig. 3b).

The accuracy of the *c*-axis orientation measurements is influenced by (i) mechanical and optical components of the FA and, (ii) the non-uniform material, i.e. boundaries, cracks or other impurities in the quartz. To check the quality of the measured *c*-axis orientations, two empirically determined values are given by the software as geometric quality and retardation quality values (Peternell et al., 2009; Fig. 3c,e)

The geometric quality (Fig. 3c) is a measure of how tightly the extinction planes (Fig. 3a) from each light direction intersect and consequently, determines the usefulness of the *c*-axis colatitude values. The geometric quality is dimensionless and ranges from 100 (excellent) to 0 (poor) (Fig. 3c). Determination of geometric quality values for each pixel of a section inside the AVA image (Fig. 3a) are presented in Fig. 3d and indicate that the *c*-axis orientation measurements inside single quartz grains are mostly reliable but become unstable towards the grain boundaries.

To evaluate the usefulness of the *c*-axis azimuths the retardation quality (Fig. 3e) is used in this study. The retardation quality is a measure of how well the phase values of the near monochromatic red, green, and blue light, from the vertical light sources (Fig. 3a), match the theoretical interference sinusoid curves of Newton's colours (Fig. 3e; Peternell et al., 2009). A value of 100 (excellent) corresponds to a perfect match of red, blue and green retardations, whereas a value of 0 (poor) corresponds to a non-reliable *c*-axis azimuth. Especially along grain boundaries the retardation quality drops down and cannot be determined locally (Fig. 3f). In this study all 10 polished and carbon coated samples were fully automated scanned with the FA. In addition, samples D47a and W39a from the Thaya dome were first uncoated and afterwards measured again. The complete measurement of one sample was performed in <1.5 h and thus the total measuring time for all 10 samples was <15 h.

5. Accuracy of the Fabric Analyser data

In a first step the accuracy of the FA was tested on the undeformed annealed Appin quartzite (Fig. 4a). Beside the accuracy this analysis was also undertaken to evaluate whether crystal impurities such as cracks or fluid and mineral inclusions influence the accuracy (Peternell et al., 2009). Automatic EBSD measurements within 13 quartz crystals show a small crystal misorientation <1.5° and for each crystal the mean *c*-axis orientation is taken as the standard orientation. The same area measured with EBSD was analysed by the FA with 2.8 μm spatial resolution (Fig. 4). To avoid misinterpretation we will use the term misorientation for differences in *c*-axis orientation within a single crystal and between different crystals and, method-related misorientation to describe the difference in *c*-axis orientation from EBSD vs. FA measurements.

5.1. Results

The coarse grained quartzite shows a well developed polygonal texture with a few fluid (FI) and mineral inclusions (I) and smaller (SC) and larger cracks (LC, Fig. 4a). The *c*-axis orientations are homogenous within each crystal (Fig. 4b), and misorientations are related to crystal impurities such as mineral inclusions and larger cracks and grain boundaries (Fig. 4a,b). Smaller cracks and fluid inclusions have no recognisable influence on the misorientations (Fig. 4a,b). The retardation and geometric quality values (Fig. 4c,d) are generally high (>80) but decrease at the impurities and towards the grain boundaries (Fig. 4a,c,d).

Between ~1000 and ~80 000 single measurements for each crystal were undertaken with the FA (Fig. 4e). It is shown that the total number of measurements suddenly decreases at combined retardation quality and geometric quality values >80 (Fig. 4e). Moreover, a cumulative *c*-axis frequency distribution in relation to EBSD vs. FA method-related misorientations reveal that less than 0.2% of all method-related misorientations are >7° and for 9 of the 13 samples more than 97% of all method-related misorientations are <5° (Fig. 4f). The FA measurement precision inside each crystal is given by the range of *c*-axis misorientations and indicated by the slope of the frequency distribution line (Fig. 4f). A precision <2° occurs for 83–99% of all *c*-axis method-related misorientation measurements (Fig. 4f). The minimum *c*-axis method-related misorientation value for each crystal is constant for retardation and geometric quality thresholds <80 (Fig. 4g) and the mean method-related misorientation remains constant for the whole threshold range (Fig. 4h). The standard deviation (σ) for the mean method-related misorientation and the maximum *c*-axis method-related misorientation for each sample show a significant decrease for quality thresholds between 70 and 80 (Fig. 4i, j). Above a threshold of ~75 method-related misorientation maxima are generally below 10–15°.

5.2. Discussion

Peternell et al. (2009, 2010) suggested a combined geometric and retardation quality threshold of >75 to filter out larger *c*-axis misorientations. Within this study we are using the same threshold because it doesn't reduce the dataset (Fig. 4e) or the minimum method-related misorientation (Fig. 4g). On the other hand, a combined geometric quality and retardation quality threshold >75 minimises the standard deviation of the mean *c*-axis method-related misorientation (Fig. 4h,i) and filters out the high method-related misorientations >10–15° (Fig. 4j).

The accuracy of the FA in comparison to EBSD is sufficiently good for CPO focused studies as method-related misorientations <7° for

99.8% of all data and <5° for 9 of 13 samples (Fig. 4f). Method-related misorientations >10–15° are mainly caused by crystal impurities such as large cracks mineral inclusions as well as proximity to the grain boundaries (Fig. 4a,b) and are filtered out by using a quality threshold of >75 (Fig. 4j). Because the FA uses transmitted light for calculating the *c*-axes the majority of the

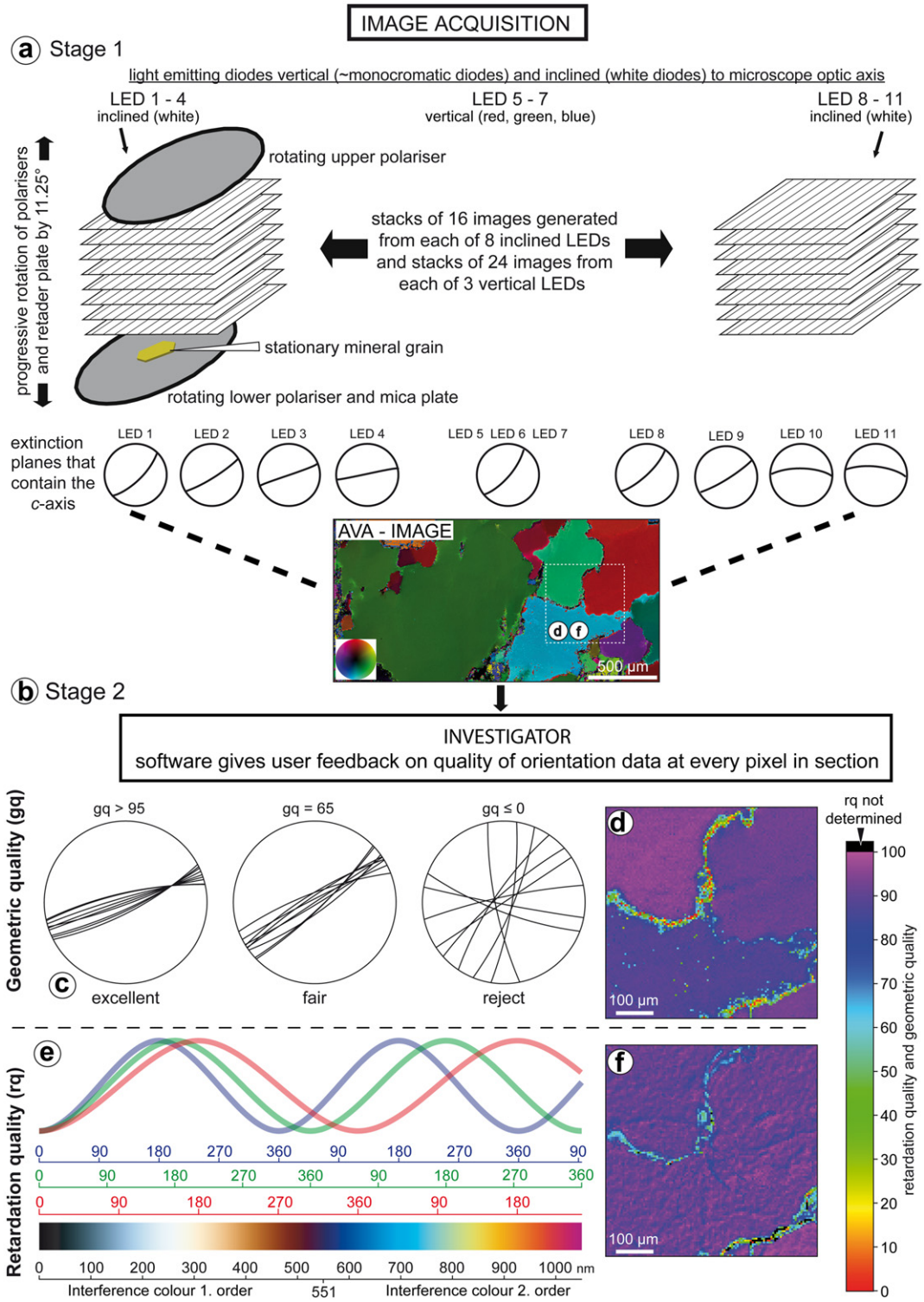

Fig. 3. Flow chart that illustrates the two-stage process performed with the FA to construct an axial-distribution (AVA) diagram and the process to evaluate the *c*-axis orientation (modified after Wilson et al., 2007): (a) Stage 1: From light sources (LED) 1–4 and 8–11 a stack of 16 images is acquired, from LED 5–7 a stack of 24 images, as the two polarisers and the retarder plate are rotated synchronously between 0° and 90° about the stationary mineral grain. The trace of the extinction plane that contains the *c*-axis with respect to the LED position is obtained from each stack and recorded. The *c*-axis orientation is determined from the 9 extinction planes and is presented in an AVA image for every pixel within the analysed area. (b) Stage 2: The data acquired from the analytical instrument are then analysed with a separate software package called INVESTIGATOR. (c) Geometric quality (gq) evaluation; excellent (gq > 95), fair (gq > 65) and rejected (gq ≤ 0); (d) geometric quality distribution map; (e) retardation quality evaluation; (f) retardation quality distribution map.

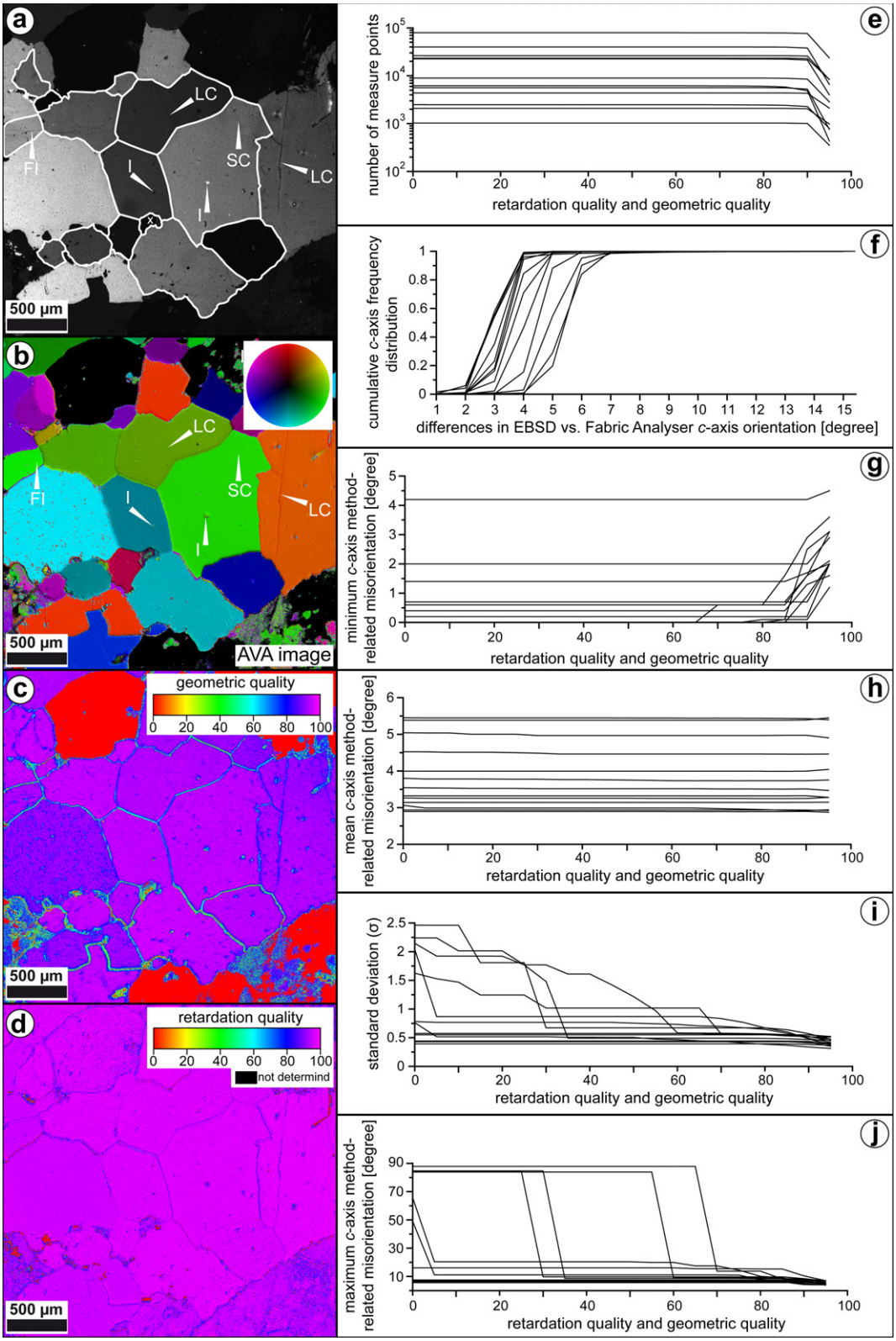

Fig. 4. Accuracy comparison between FA and EBSD *c*-axis orientation measurements undertaken on an undeformed quartz sample from the Appin quartzite (sample 35A, courtesy of H. Bergman). (a) Typical microstructure of the studied Appin Quartzite. Quartz grains are statistically recrystallised with polygonal shapes and straight boundaries meeting in triple point junctions (1000 × 1000 px large crossed polariser microphotograph), Analysed quartz crystals are outlined (white line); X marks a crystal that was not analysed. White arrows are pointing to internal impurities in the quartz crystals, FI = fluid inclusion, I = mineral inclusion, SC = small crack and LC = large crack. (b) Axial distribution analysis (AVA) image from (a); *c*-axes are colour labelled regarding to the lockup table. (c) Geometric quality distribution map; (d) retardation quality distribution map. Note decrease of the measurement quality at crystal impurities and towards grain boundaries. (e–j) Statistical evaluation of EBSD vs. FA *c*-axis method-related misorientation measurements in form of line plots showing the relation between quality results quality (retardation and geometric quality) and (e) number of measure points; (g) minimum, (h) mean, (i) standard deviation, (j) maximum difference between *c*-axis orientations using both methods.

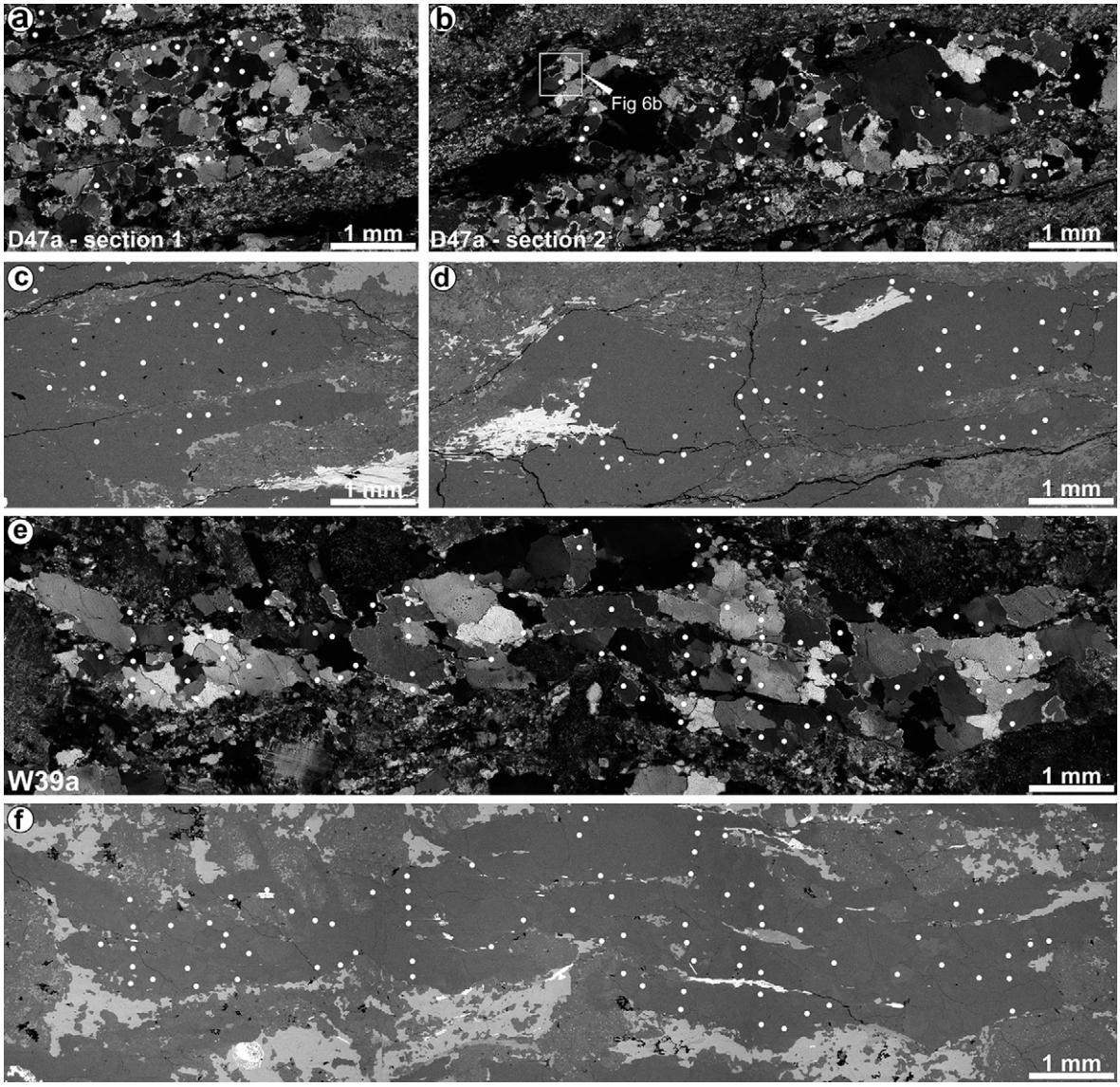

Fig. 5. Photomicrographs and SEM images of quartz lenses showing the position of EBSD and FA measurements. (a–b) Photomicrographs and (c–d) SEM images from recrystallised quartz lenses of sample D47a; (e–f) photomicrograph and SEM image from a recrystallised quartz lens of sample W39a. White circles indicate position of EBSD and FA measurements. Circle diameter is ten times the electron beam diameter for the EBSD measurements. White rectangle indicates position of area shown in Fig. 6b.

higher method-related misorientations (~5–7°) might be related to small crystal impurities also located inside the crystal. Such internal impurities do not influence the EBSD measurements. Misorientations related to these small internal crystal impurities cannot be filtered automatically with the currently used FA.

In the case of the Appin quartzite the misorientation within a single crystal is <2° and <1.5° measured with the FA (Fig. 4f) and EBSD respectively. This reveals the high precision of the FA. The applicability of the FA to measure very small crystal-internal *c*-axis misorientations (<1°) was not investigated within this study. Therefore, EBSD is seen as the favourable method for such highly accurate analysis. However, these very high accuracies are only required in very specific cases, e.g. analysing subgrain relationships. For standard quartz texture analysis, i.e. analysing the bulk texture of quartz domains the FA accuracy is sufficiently high.

6. EBSD and Fabric Analyser point to point comparison

Well–equilibrated monomineralic rocks (as the Appin quartzite) are very useful to test the FA accuracy, but most rocks are polymineralic and reveal a complex deformation history recorded in the mineral textures. Therefore, to evaluate the accuracy of the FA in deformed and polymineralic rocks the same points within single quartz crystals were measured with both, EBSD and FA in two representative orthogneiss samples (D47a and W39a; Fig. 5).

Quartz grains in the Thaya orthogneiss sample (D47a) are finer-grained (200–400 μm) than those from the Weitersfeld orthogneiss (W39a; 300–800 μm). Initially, the measured points are defined by EBSD measurements and afterwards measured by the FA. Both systems use a digital camera with a specific pixel resolution for capturing the back scatter image in case of EBSD and the crossed polariser images in case of the FA. These pixel images define the two grids shown in Fig. 5 and each point measurement is spatially related to a certain position within the grid and binned to the grid's spatial resolution. As both systems analyse the *c*-axis orientations with a slightly different spatial resolution the measured points do not usually match perfectly (Fig. 6). The sketch in Fig. 6a illustrates how a measured point from the FA (grey rectangle) was chosen based on a given EBSD point (black rectangle). To enable repeatable and objective selection criteria for the

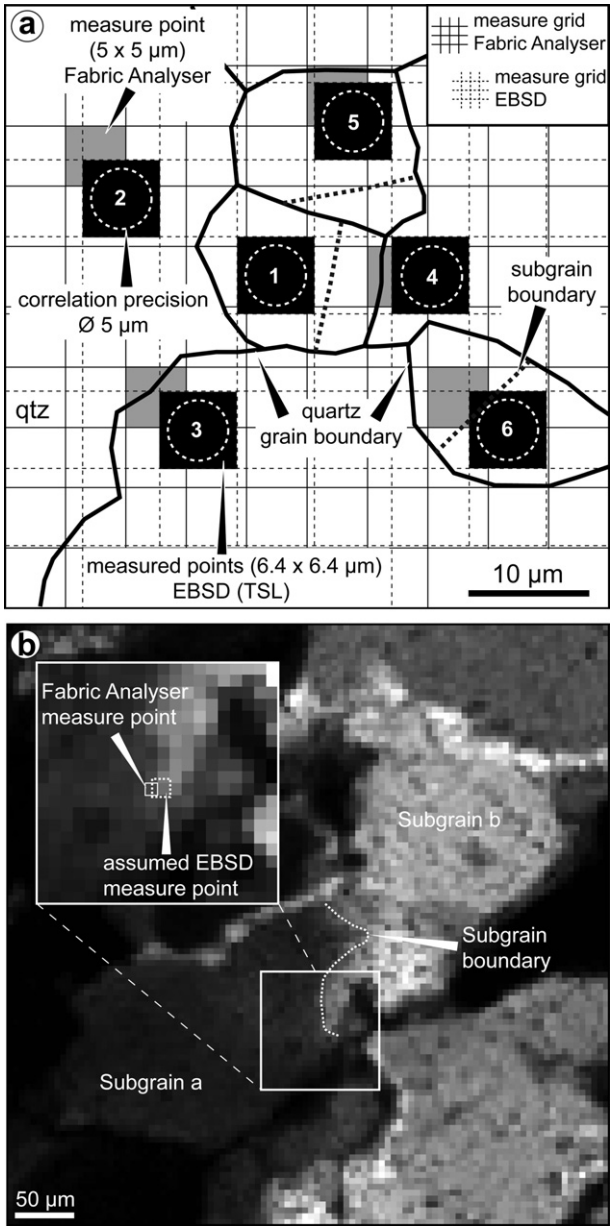

Fig. 6. Principles of EBSD vs. FA point to point comparison. (a) Overlapping measurement grids obtained from the EBSD (black rectangles) and FA (grey rectangles). One EBSD measurement point can be correlated with FA point using the precision circle (dashed circle). Point 1–6 show different possible positions of these circles (for details see text). Points measured by FA and EBSD with spatial resolution of 5 µm/pixel and 6.4 µm/pixel, respectively. (b) Example for *c*-axis misorientation related to a subgrain boundary from sample D47a-section 2 (Fig. 5b). The misorientation between the 2 subgrains measured by the FA = 17°. The method-related misorientation between FA and EBSD = 19°. EBSD measurement point can only be assumed.

selection of the measure points from the FA a correlation circle (white dashed circle) with a diameter of 5 µm is placed into the centre of each EBSD measure point (Fig. 6a). A 5 µm diameter for the correlation circle is chosen because of the FA related AVA image resolution. All grid points from the FA grid intersecting with a circle are potential measurement points and the convention is to use always the upper left or in case of point 4 (Fig. 6a) the left grid points for the point to point comparison. Thus, the maximum distance between a single EBSD and FA measurement point centre is <16 µm. Point 1 (in Fig. 6a) shows the ideal case where the correlation circle intersects just with a single grid point from the AVA image. Nevertheless, in most cases the circle intersects with 2–4 grid points (Fig. 6a, points 2–6). Depending on the location of the EBSD points within a single quartz crystal the FA measurement point is intersected by a grain boundary (Fig. 6a, points 3–5) or both points lie within different subgrains of the same crystal (point 6). This situation is illustrated in Fig. 6b where an FA measured point lies very close to a subgrain boundary. The misorientation between both sides of the boundary is 17 ± 2° (measured with the FA). The EBSD position cannot be exactly determined in relation to the FA point but lies within 16 µm distance. As the EBSD vs. FA *c*-axis method-related misorientation for this measure point = 19° it is most likely that both measured points are located in two different subgrains (Fig. 6b, insert).

6.1. Results

In case of the finer grained Thaya orthogneiss sample D47a (Fig. 4a–d) the differences in *c*-axis orientation related to the geometric quality (Fig. 7a,c) and the retardation quality (Fig. 7b,d) are in general similar for the carbon coated and the uncoated samples. A maximum in *c*-axis method-related misorientation between FA and EBSD measurements <15° occurs for geometric and retardation qualities >75 (Fig. 7a–d). Method-related misorientations >15° are related to geometric qualities between 25 and 85 for the carbon coated sample (Fig. 6a) and between 0–30 and 55–95 for the uncoated sample (Fig. 7c). *c*-axis differences >15° are related to retardation qualities of >80 (Fig. 7b,d) with few measurements <85. Retardation values = 0 are rejected measurements.

The coarser grained Weitersfeld orthogneiss sample W39a (Fig. 5e–h) reveals similar results. Only in the case of W39a with a carbon coating the data points are more scattered outside the clear maximum (Fig. 7e). A frequency distribution of *c*-axis method-related misorientations from the FA vs. EBSD in relation to a quality threshold is shown in Fig. 8. The different frequency distribution diagrams are related to combined thresholds for the geometric and retardation quality of ≥75. The frequency distribution for the carbon coated and uncoated sample D47a are slightly different (Fig. 8a, b). For a quality threshold of ≥75 the histogram in Fig. 8a is almost symmetric with a maximum around the average method-related misorientation in EBSD and FA *c*-axis distribution of 6.5°. The frequency distribution diagrams from the uncoated D47a (Fig. 8b) show a weak bimodal distribution with two maxima in method-related misorientation <3° and >8° with an average of 5.9°.

In the case of the carbon coated sample W39a the histogram is weakly asymmetric with a maximum of 2–4° and an average of 4.9° (Fig. 8c). The frequency distribution in case of the uncoated sample W39a shows a concentration of almost all values between 1 and 7° with an average of 3.8°.

6.2. Discussion

The results of point to point comparison between EBSD and FA measurements lead to a sufficient correlation of 3.8°–6.5° (Fig. 8) of method-related misorientations <15° (Fig. 7). Almost all of the measured points with differences in *c*-axis orientation between EBSD and FA <15° are related to combined geometric and retardation qualities >75, which are consistent with the results from the undeformed Appin quartzite (Fig. 4j). Nevertheless, the method-related misorientation interval of 0–15° in the Thaya samples is significantly larger than for the quartzite (0–7°, Fig. 4f). These larger method-related misorientations in W39a and D47 are most likely related to crystal impurities, grain boundaries and subgrains (Fig. 6b). Similar to the discussion in section 5.2 some of these impurities are inside the crystal and therefore influence only the FA measurements. Nevertheless the larger number of these higher method-related misorientations are also caused by the mismatch of

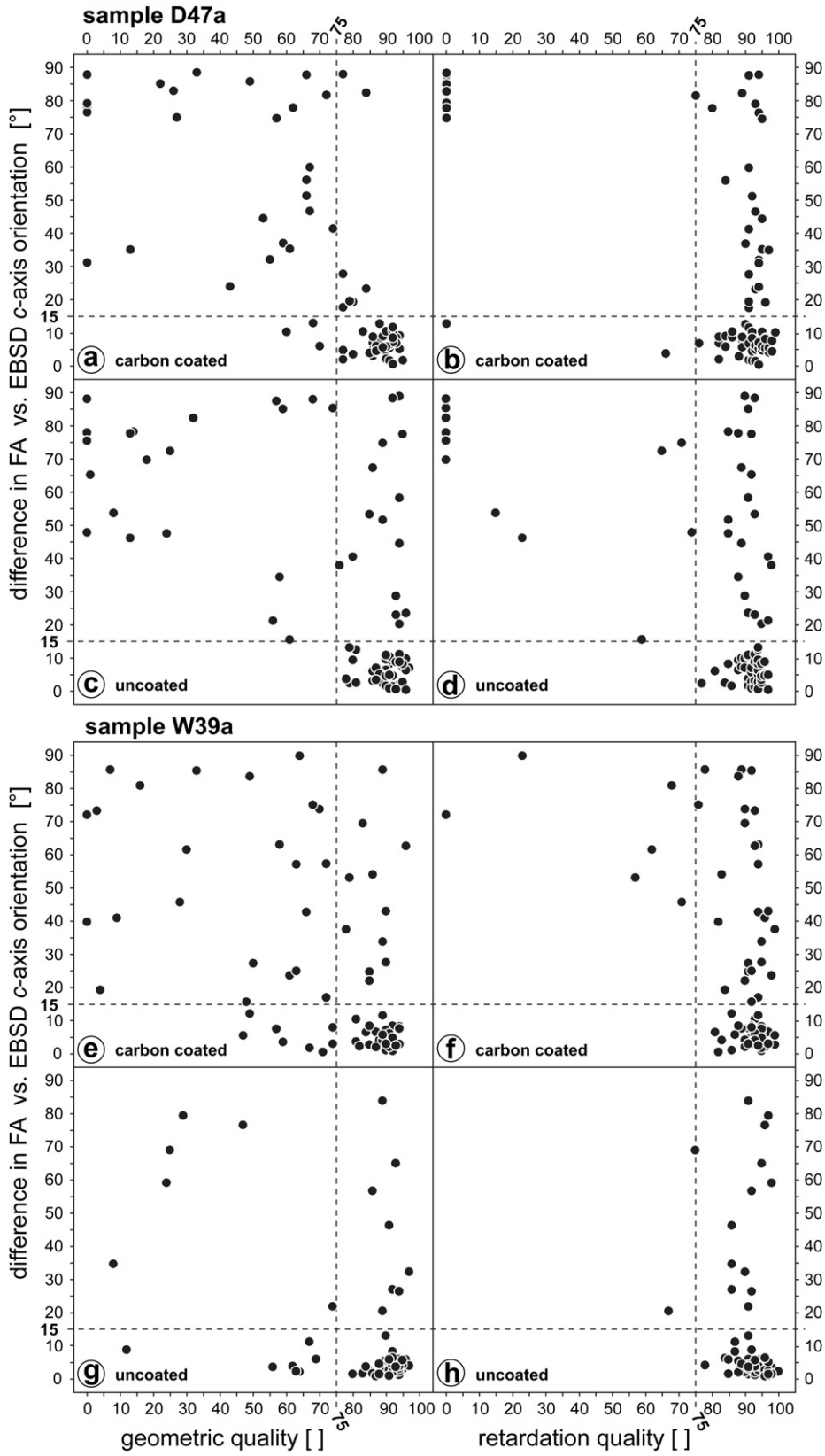

Fig. 7. Comparison of the *c*-axis orientation of EBSD and FA measurements vs. geometric and retardation quality from same measure points inside two thin sections: D47a (a–d) and W39a (e–h); Results from carbon coated samples (a, b, e, f) and from uncoated samples (c, d, g, h) are distinguished. Dashed line marks quality thresholds (further discussed in text); 78 points in both samples were analysed.

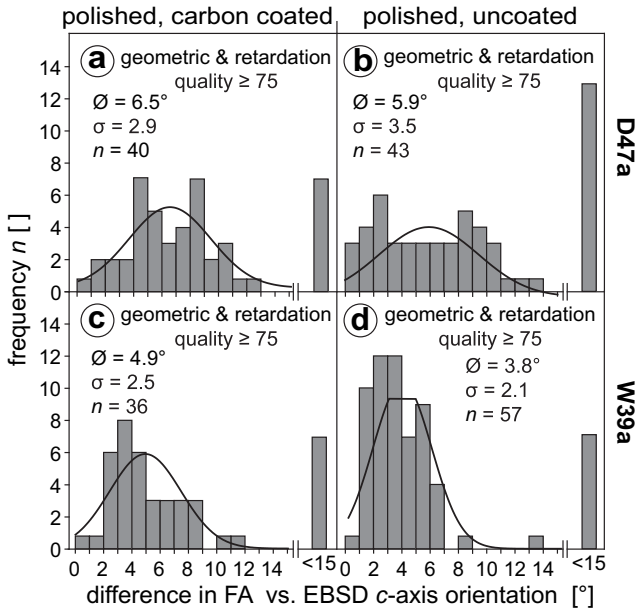

Fig. 8. Differences in *c*-axis orientation from same measured points in FA and EBSD expressed as frequency distribution histograms. (a–b) sample D47a; (c–d) sample W39a. Results from carbon coated samples (a, c) and from uncoated samples (b, d) are distinguished. *N* indicates the total number of single measurements with a difference in *c*-axis orientation between 0° and 15°; Ø = average value of difference in *c*-axis orientation; σ = standard deviation; black solid line represents the best Gaussian distribution fit.

similar EBSD and FA measurement points of <16 μm (Figs. 5 and 6). In the finer grained sample D47 this mismatch increases as the probability to measure impurities or grain boundaries is higher. This is shown as a larger number of *c*-axis method-related misorientations between 7° and 15° in comparison to the coarser grained sample W39a (Fig. 8). Thus, the average method-related misorientations of <6.5° for sample D47a (Fig. 8a,b) and <4.9° for sample W39a (Fig. 8c,d) are upper limits affected by a combination of an imprecise comparison method between the FA and EBSD (Fig. 6a), crystal impurities and deformation (Fig. 6b). The results confirm the good accuracy of the FA and its applicability for a fast single grain analysis in polymineralic rocks.

Carbon coating dilutes the transmitted light of the FA having minor influence on the *c*-axis orientation and resulting in an average method-related misorientation below 1.1° between the carbon coated and the uncoated samples (Fig. 8). This small method-related misorientation indicates that carbon coating is not the main factor for the differences in *c*-axis orientations (Fig. 7a–d), which is in accordance to the observations by Wilson et al. (2003, 2007) and Peternell et al. (2009) that polished, unpolished and stained thin sections as well as etched and unetched fission track mounts can be used by the FA. Nevertheless, in the more coarse grained sample W39a (Fig. 7e–h) most of the high-angle differences in *c*-axis orientations (i.e. >15°), together with low qualities values (i.e. <75), occur only within the carbon coated sample (Fig. 6e,f). Thus, in combination with lower quality measurements larger numbers of method-related misorientations are more likely in carbon coated samples.

7. Comparison of quartz textures from the whole thin sections

To compare FA and EBSD measurements on a larger statistical base, EBSD and FA *c*-axis orientation measurements within 9 thin sections were performed (Fig. 9). To avoid inaccuracies, measurements for both systems are performed manually. EBSD measured points are selected from back scatter images and evaluated by the match of the observed Kikutchi patterns with the theoretical models for quartz. FA measurement points are selected from the AVA images and only points inside a crystal are chosen with a combined geometric and retardation quality >75.

7.1. Results

In most cases, FA and EBSD results are almost identical (Fig. 9). Nevertheless, small differences in the pole figures as in samples D46b or W16 occur (Fig. 9). In the case of sample D21b the quartz *c*-axis orientation obtained from EBSD and FA illustrated significant differences, where results from EBSD reveal an asymmetric single maximum close to the centre of diagram in contrast to the two maxima obtained by the FA (Fig. 9; section 8).

The quartz measurements from the three orthogneisses result in different *c*-axis patterns (Fig. 9) that reflect different quartz microstructures (Fig. 2). The stereonets showing *c*-axis orientations are accordingly sorted by the metamorphic grade from highest Bíteš orthogneiss to lowest Thaya orthogneiss (Figs. 2 and 9). For the high temperature Bíteš orthogneiss, quartz *c*-axis maxima forms an incomplete and slightly asymmetric type II cross girdle with an opening angle of ~90° (sample B5) or single, slightly asymmetric girdle (sample B12; Fig. 9). The position of *c*-axis maxima indicates basal <a> and rhomb <a + c> slip with some contribution of prism <c> slip-systems. The relative medium temperature deformed Weitersfeld orthogneiss (samples W16, W39a and W40) reveals an oblique single girdle indicating mainly activity of basal <a> and rhomb <a + c> slip-systems with less frequently prism <a> slip. Quartz pattern from the lower temperature Thaya orthogneiss (samples D47a, D46b, D50a and D21b) show either maxima close to the centre of the diagram, or a single girdle indicating dominance of prism <a> slip (D50a, D21b) with minor contribution of basal <a> and rhomb <a + c> slip-systems that were dominant in the previous Weitersfeld orthogneiss.

7.2. Discussion

As shown above, quartz *c*-axis pattern changes systematically from basal <a> and rhomb <a + c> slip-systems in high temperature Bíteš orthogneiss, rhomb <a + c> and basal <a> slip-systems in the Weitersfeld orthogneiss to dominantly prism <a> slip in low grade Thaya orthogneiss (Fig. 9). This sequence is commonly interpreted as a result of increasing temperature plasticity but is in contrast to high temperature microstructures in the Bíteš orthogneiss, lower temperature ones in the Weitersfeld orthogneiss and lowest temperatures in the Thaya orthogneiss (Fig. 2) as determined using petrological tools (section 3.1).

Stipp et al. (2002) studied deformed quartz veins in contact aureole of Adamello intrusion and have shown that *c*-axis girdle pole figures that are a result of combined basal, rhomb and prism <a> slip-systems change to single maxima in Y (cause by prism <a> slip) at the subgrain boundary rotation recrystallisation and grain boundary migration transition at about 500 °C. The Thaya orthogneisses shows subgrain boundary rotation recrystallisation at temperatures ~500 °C (Fig. 2). The Weitersfeld orthogneisses and the Bíteš orthogneiss show increasing recrystallisation temperatures of ~600° and ~650°, respectively. The latter one is in coincidence with an opening angle of ~90° (Kruhl, 1998; Morgan and Law, 2004) and shown by the incomplete cross girdle in sample B5 (Fig. 9). With increasing temperature grain boundary migration recrystallisation in quartz becomes the dominant process (Fig. 2). Nevertheless, in contrast to the results

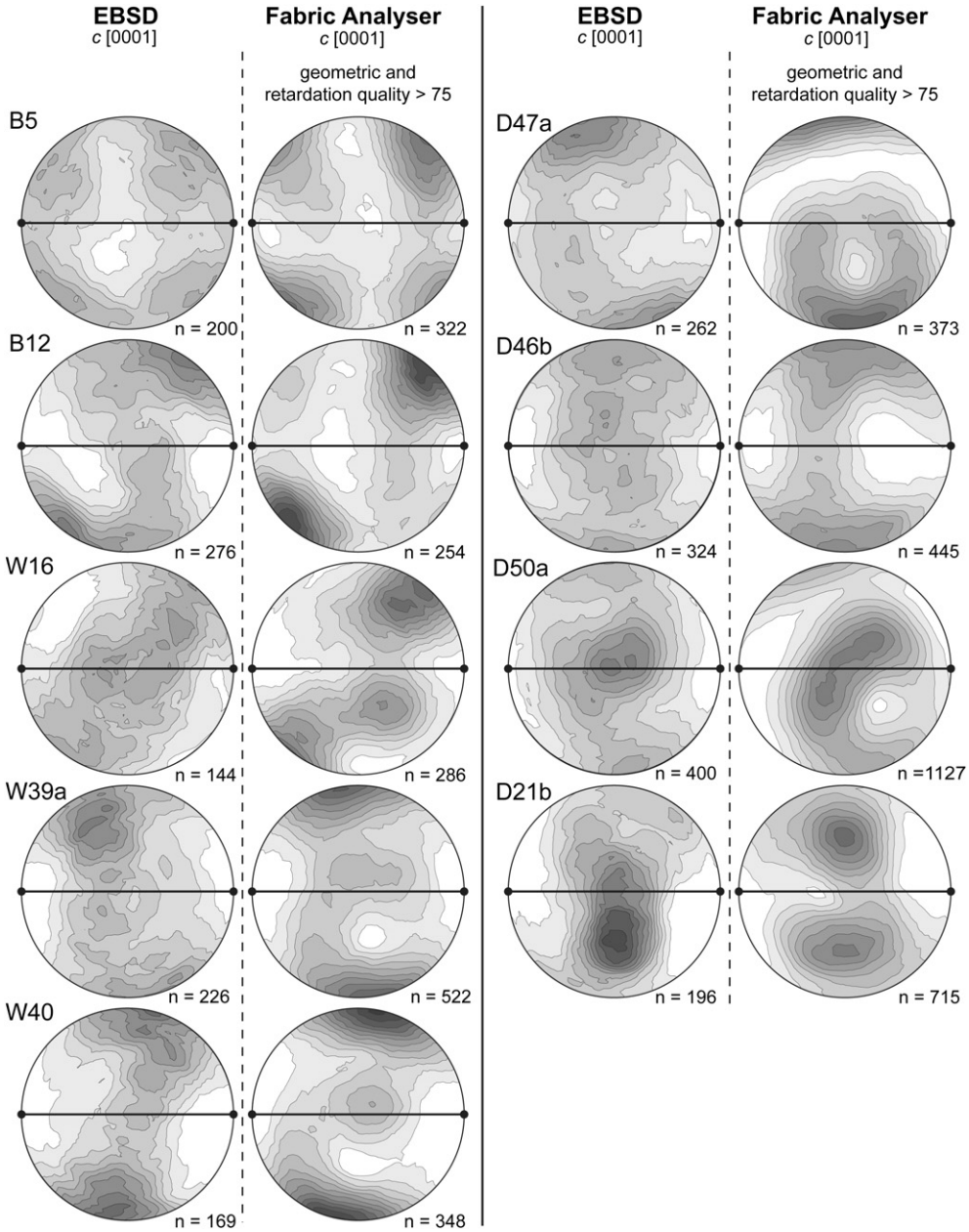

Fig. 9. Crystallographic preferred orientations (CPO) of quartz measured with EBSD and the FA in Bíteš, Weitersfeld and Thaya orthogneiss. The stereonets are sorted by the metamorphic grade from highest Bíteš orthogneiss sample B5 to the lowest Thaya orthogneiss sample D21b. The FA results are also represented in relation to a geometric and retardation quality threshold >75. Equal area projections, lower hemisphere, contoured at interval of 0.3 times uniform distribution. Foliation is horizontal (black solid line) and lineation is in the plane in the E–W direction (black circles). The number of quartz analysis (*n*) in each sample is shown.

from Stipp et al. (2002) the quartz textures show prism <a> slip for the lowest temperatures (D50a, D21b) and combined basal, rhomb and prism <a> slip for the higher temperature deformed samples (Fig. 9). The *c*-axis orientation patterns from the observed orthogneisses are also in conflict to Schmid and Casey (1986) who suggest prism <a> slip in quartz is the dominant slip-system at high temperatures and/or high strain rates. What is the reason for such an inverse sequence? In case of the Thaya Dome, quatz and feldspar microstructures (section 3.1, Fig. 2) and the results from section 8 indicate that the formation of quartz *c*-axis preferred orientations is not only controlled by temperature but also by deformation mechanism, e.g. strain and/or strain rate partitioning mainly dominated by the relative weak feldspar matrix (section 8). Therefore, *c*-axis preferred orientations from the Thaya Dome demonstrate the importance of microstructural analysis of both quartz and feldspar in such quartzo-feldspathic rocks and, in combination with petrological observations.

8. Variation in quartz *c*-axis orientation patterns on the thin section scale

In order to evaluate changes in the *c*-axis within a single thin section five recrystallised quartz lenses of sample D21b were measured with the FA and the data are then compared to EBSD measurements from two of the five quartz lenses (Fig. 10).

Results from EBSD show an asymmetric single maximum close to the centre of diagram in contrast to the two maxima obtained by the FA (sample D21b, Fig. 9). Detailed quartz *c*-axis orientation

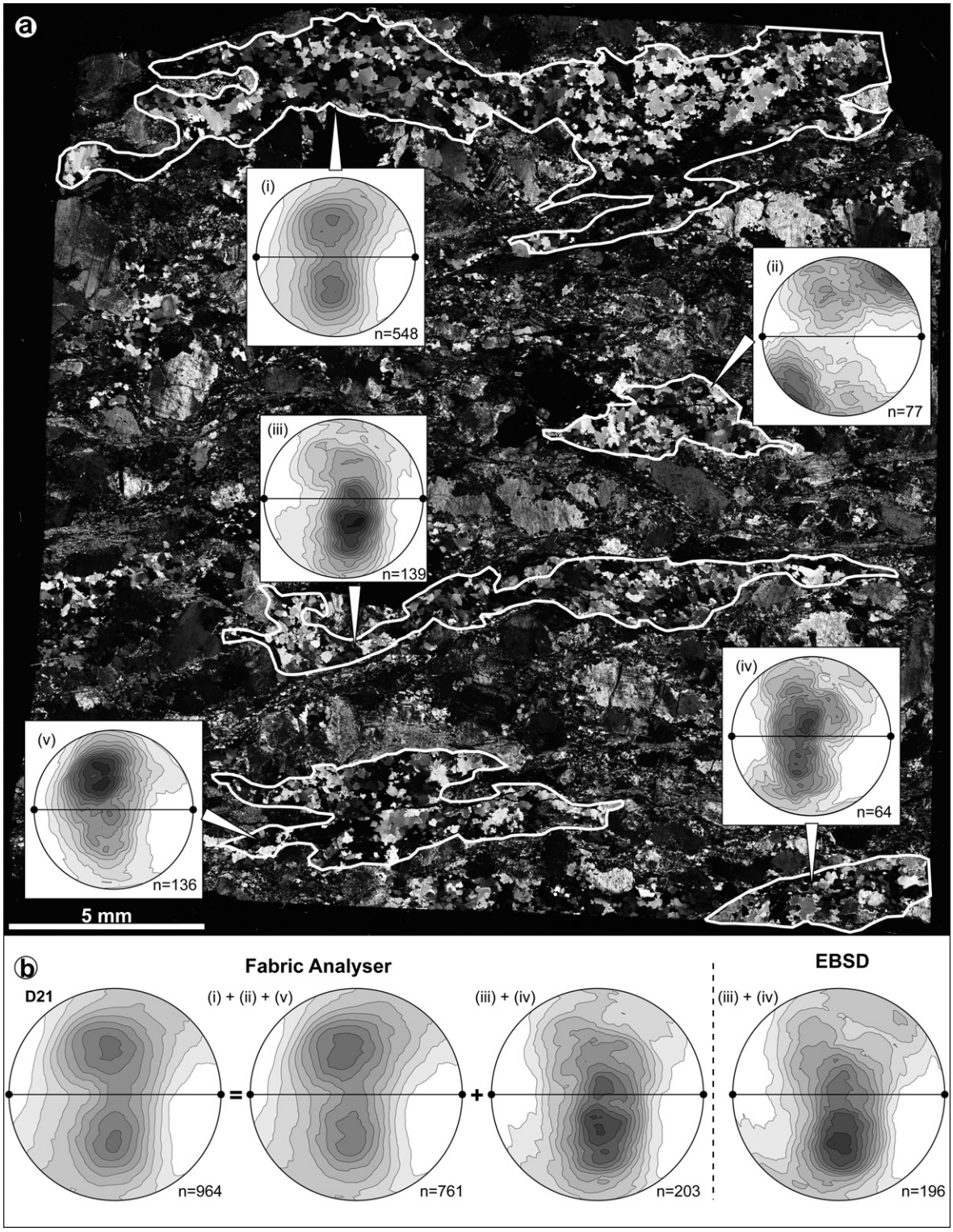

Fig. 10. Variation in quartz *c*-axis orientation patterns on the thin section scale (sample D21b). (a) Microphotograph with outlined analysed quartz ribbons with attached *c*-axis orientation stereonet plots for each ribbon. Each ribbon reveals different *c*-axis pattern. (b) Stereonet plots explaining the origin of different quartz CPO pattern measured by EBSD and FA. Equal area projections, lower hemisphere, contoured at interval of 0.3 times uniform distribution. Foliation is horizontal (black solid line) and lineation is in the plane in the E–W direction (black circles). *N* indicates number of quartz analysis in each sample.

measurements (Fig. 10a) from lens (i) and (iv) form a broad band with two symmetric distributed maxima indicating active rhomb and prism <a> slip. The *c*-axis pattern from lens (iii) and (v) consist of a broad band with a single asymmetric maximum in case of lens (iii) close to Y (prism <a> ± rhomb <a + c> slip) and at ~45° away from Y (rhomb <a + c> ± prism <a>). In contrast, the *c*-axis orientations of lens (ii) form an incomplete and asymmetric cross girdle with the maxima indicating dominant basal <a> slip. The FA *c*-axis pole figure including all measurements (Fig. 9) can be constructed by merging the results from each lens together (Fig. 10b).

The merged *c*-axis texture from merging pole figure (iii) and (iv) is identical to the results from the EBSD performed on the same quartz lenses (Fig. 10b).

The Thaya orthogneiss sample D21b is naturally deformed at ~500 °C and quartz recrystallisation is controlled by subgrain boundary recrystallisation (Fig. 2). Deformation partitioning seems to be the controlling factor for the heterogeneity in quartz *c*-axis preferred orientations within the sample. Importance of deformation partitioning for interpretations of deformation mechanism and kinetics was already discussed by many authors (e.g. Knipe and Law, 1987; Pauli et al., 1996; Schulmann et al., 1996). The Thaya orthogneiss samples emphasise that not only bulk microstructures should be taken in account, but also individual domains should be assessed separately, because of their different fabrics. Several authors emphasized the role of finite strain intensity on the transient character of mineral textures in monomineralic mylonites (Herwegh et al., 1997; Heilbronner and Tullis, 2006). The latter authors show that the basal <a> slip is characteristic for low strain intensities while the prism <a> reflects high strain component. Our study reflects similar evolution but related to various degree of strain partitioning related to the weak feldspar matrix activity (e.g. mentioned by Jeřábek et al., 2007). Because of its fast performance and its ability to measure quartz *c*-axes direct on microphotographs, the FA is an ideal tool to determine such heterogeneities in strain on the thin section scale.

9. Conclusions

Comparison between EBSD and FA bulk quartz *c*-axis orientations using different methods lead to almost identical results. Moreover, single point *c*-axis orientation measurements show good angular accuracy of the FA. The average method-related misorientations between the two methods are in the range of 2.9°–5.5° in case of the Appin quartzite and 3.8°–6.5° for the Thaya orthogneisses. Using the FA in the Appin quartzite the measured misorientation across a single grain is <2° similar to the results from EBSD analysis on the same grains. Larger spread in measured misorientations and method-related misorientations is related to crystal impurities, subgrains boundaries and the spatial inaccuracy of the point to point comparison method. No special sample preparation is needed in the case of the FA, up to 10 × 10 cm sized uncovered polished or carbon coated samples can be used with the same quality results. However, only uniaxial minerals can be measured. FA geometric and retardation quality values are used to evaluate each *c*-axis orientation. A combined threshold for these values >75 lead to highest accuracy of the orientation data.

The FA can determine quartz CPOs of a whole thin section within <45 min (50 μm/pixel resolution), <1.5 h (5 μm/pixel resolution) or <8 h (2.8 μm/pixel resolution) and therefore, offers the only possibility to analyse whole thin sections with such a spatial resolution of 2.8–50 μm and sufficient accuracy for CPO based studies in a reasonable short time. Therefore, large datasets and texture heterogeneities within the thin section scale can be easily analysed. Consequently, the FA offers a relatively inexpensive but still accurate alternative to classical EBSD *c*-axis measurements in quartz.

Quartz CPOs from the Thaya orthogneisses reveal a clear trend from basal <a> and rhomb <a + c> slip for high temperature, rhomb <a> and basal <a> slip for medium temperature and prism <a> slip for low temperature orthogneisses. This is a reversal of the sequence normally attributed to temperature and indicates that quartz texture forming process is controlled by deformation rather than by temperature. Furthermore, this reverse textural evolution on a regional scale has an important impact for textural interpretation in polymineralic rocks, i.e. as feldspar seems to be the controlling factor for deformation partitioning. The results from the Thaya orthogneisses suggest that in rocks which have undergone a complicated tectonometamorphic history, a robust interpretation of quartz *c*-axis orientations is necessary to enable an estimation of deformation temperatures and/or to determine deformation partitioning in polymineralic rocks. In particular in quartzo-feldspatic rocks deformation partitioning causing heterogeneities in activated deformation mechanisms and slip systems of quartz seems to be more widespread than previously thought.

Acknowledgments

This work was financially supported by the grant from French National Agency (No. 06–1148784 to KS), Australian Research Grant (No. Dl 0773097 to MP and CW), the European Science Foundation (EUROCORES Programme, EuroMinSci, MinSubStrDyn, No. ERAS-CT-2003-980409 of the European Commission, FP6 to SP). We also thank the Knut och Alice Wallenberg stiftelse for funding of the experimental setup. We would like to thank Patricie Týcová from Czech Geological Survey for careful preparation of the samples for EBSD measurements. Helena Bergman from Stockholm University is thanked for the provision of the Appin Quartzite sample. We also thank Steve Reedy for his valuable review with many constructive comments and suggestions for improving this paper, and the Journal editor C. Passchier for his careful handling of the manuscript.

References

Adams, B.L., Wright, S.I., Kunze, K., 1993. Orientation imaging: the emergence of a new microscopy. Metallurgical and Materials Transactions A 24, 819–831.
Bailey, E.H., Stevens, R.H., 1960. Selecting straining of K-feldspar and plagioclase on rock lobes and thin sections. American Mineralogist 45, 1020–1025.
Bascou, J., Barruol, G., Vauchez, A., Mainprice, D., Egydio-Silva, M., 2001. EBSD-measured lattice-preferred orientations and seismic properties of eclogites. Tectonophysics 342, 61–80.
Berek, M., 1924. Mikroskopische Mineralbestimmung mit Hilfe der Universaldrehtischmethode. Gebrüder Borntraeger, Berlin.
Blumenfeld, P., Mainprice, D., Bouchez, J.L., 1986. C-slip in quartz from subsolidus deformed granite. Tectonophysics 127, 97–115.
Buntebarth, G., Voll, G., 1991. Quartz grain coarsening by collective crystallization in contact quartzites. In: Voll, G., Topel, J., Pattison, D.R.M., Seifert, F. (Eds.), Equilibrium and Kinetics in Contact Metamorphism: The Ballachulish Igneous Complex and its Aureole. Springer Verlag, Heidelberg, pp. 251–266.
Dell'Angelo, L.N., Tullis, J., 1989. Fabric development in experimentally sheared quartzites. Tectonophysics 169, 1–21.
Dudek, A., 1980. The crystalline basement block of the outer Carpathians in Moravia; Bruno-Vistulicum. Rozpravy Československé Akademie 90, 85.
Fairbairn, H.W., 1949. Structural Petrology of Deformed Rocks. Addison-Wesley Press Inc., Cambridge.
Fueten, F., 1997. A computer-controlled rotating polarizer stage for the petrographic microscope. Computers & Geosciences 23, 203–208.
Fueten, F., Goodchild, J.S., 2001. Quartz *c*-axis orientation determination using the rotating polarizer microscope. Journal of Structural Geology 23, 895–902.
Fynn, G.W., Powell, W.J.A., 1979. The Cutting and Polishing of Electro-Optic Materials. Institute of Physics Publishing, Bristol.
Gleason, G.C., Tullis, J., Heidelbach, F., 1993. The role of dynamic recrystallization in the development of lattice preferred orientations in experimentally deformed quartz aggregates. Journal of Structural Geology 15, 1145–1168.
Hasalová, P., Schulmann, K., Lexa, O., Štípská, P., Hrouda, F., Ulrich, S., Haloda, J., Týcová, P., 2008. Origin of migmatites by deformation-enhanced melt infiltration of orthogneiss: a new model based on quantitative microstructural analysis. Journal of Metamorphic Geology 26, 29–53.
Heilbronner, R.P., Pauli, C., 1993. Integrated spatial and orientation analysis of quartz *c*-axis by computer-aided microscopy. Journal of Structural Geology 15, 369–382.
Heilbronner, R., Tullis, J., 2006. Evolution of *c*-axis pole figures and grain size during dynamic recrystallization; results from experimentally sheared quartzite. Journal of Geophysical Research 111, B10202.
Herwegh, M., Handy, M.R., Heilbronner, R., 1997. Temperature- and strain-rate-dependent microfabric evolution in monomineralic mylonite: evidence from in situ deformation of norcamphor. Tectonophysics 280, 83–106.
Hobbs, B.E., 1968. Recrystallization of single crystals of quartz. Tectonophysics 6, 353–401.
Jeřábek, P., Stünitz, H., Heilbronner, R., Lexa, O., Schulmann, K., 2007. Microstructural deformation record of an orogen-parallel extension in the Vepor Unit, West Carpathians. Journal of Structural Geology 29, 1722–1743.

Ji, S., Mainprice, D., 1988. Natural deformation fabrics of plagioclase: implications for slip systems and seismic anisotropy. Tectonophysics 147, 145–163.
Knipe, R.J., Law, R.D., 1987. The influence of crystallographic orientation and grain boundary migration on microstructural and textural evolution in an S–C mylonite. Tectonophysics 135, 155–169.
Kruhl, J.H., 1998. Reply: prism- and basal-plane parallel subgrain boundaries in quartz a microstructural geothermobarometer. Journal of Metamorphic Geology 16, 142–146.
Lloyd, G.E., Schmidt, N.H., Mainprice, D., Prior, D.J., 1991. Crystallographic textures. Mineralogical Magazine 55, 331–345.
Menegon, L., Pennacchioni, G., Heilbronner, R., Pittarello, L., 2008. Evolution of quartz microstructure and c-axis crystallographic preferred orientation within ductilely deformed granitoids (Arolla unit, Western Alps). Journal of Structural Geology 30, 1332–1347.
Morgan, S.S., Law, R.D., 2004. Unusual transition in quartzite dislocation creep regimes and crystal slip systems in the aureole of the Eureka Valley-Joshua Flat-Beer Creek pluton, California: a case for anhydrous conditions created by decarbonation reactions. Tectonophysics 384, 209–231.
Mørk, M.B.E., Moen, K., 2007. Compaction microstructures in quartz grains and quartz cement in deeply buried reservoir sandstones using combined petrography and EBSD analysis. Journal of Structural Geology 29, 1843–1854.
Pattison, D.R.M., Harte, B., 1997. The geology and evolution of the Ballachulish igneous complex and aureole. Scottish Journal of Geology 33, 1–29.
Pauli, C., Schmid, S.M., Heilbronner, R., 1996. Fabric domains in quartz mylonites: localized three dimensional analysis of microstructure and texture. Journal of Structural Geology 18, 1183–1203.
Peternell, M., Bitencourt, M.F., Kruhl, J.H., Stäb, C., 2010. Macro and microstructures as indicators of the development of syntectonic granitoids and host rocks in the Camboriú region, Santa Catarina, Brazil. Journal of South American Earth Sciences 29, 738–750.
Peternell, M., Kohlmann, F., Wilson, C.J.L., Seiler, C., Gleadow, A.J.W., 2009. A new approach to crystallographic orientation measurement for apatite fission track analysis: Effects of crystal morphology and implications for automation. Chemical Geology 265, 527–539.
Prior, D.J., 2009. EBSD in the earth sciences: application, common practice and challenges. In: Schwartz, A.J., Kumar, M., Adams, B.L., Field, D.P. (Eds.), Electron Backscatter Diffraction in Materials Science. Springer Science and Business Media, New York, pp. 345–360.
Prior, D.J., Boyle, A.P., Brenker, F., Cheadle, M., Day, A., Lopez, G., Peruzzo, L., Potts, G.J., Reddy, S., Spiess, R., Timms, N.E., Trimby, P., Wheeler, J., Zetterström, L., 1999. The application of electron backscatter diffraction and orientation contrast imaging in the SEM to textural problems in rocks. American Mineralogist 84, 1741–1759.
Prior, D.J., Wheeler, J., 1999. Feldspar fabrics in a greenschist facies albite-rich mylonite from electron backscatter diffraction. Tectonophysics 303, 29–49.
Reinhard, M., 1931. Universal-Drehtischmethode. B.Wedf & Cie, Basel.
Romeo, I., Capote, R., Lunar, R., Cayzer, N., 2007. Polymineralic orientation analysis of magmatic rocks using electron back-scatter diffraction: implications for igneous fabric origin and evolution. Tectonophysics 444, 45–62.
Sander, B., 1930. Gefügekunde der Gesteine. Springer-Verlag, Wien.
Sander, B., 1950. Einfuehrung in die Gefuegekunde der Geologischen Koerper; Zweiter Teil, Die Korngefuege. Springer-Verlag, Wien-Innsbruck.
Schmid, S.M., Casey, M., 1986. Complete fabric analysis of some commonly observed quartz [c]-axis patterns. In: Hobbs, B.E., Heard, H.C. (Eds.), Mineral and Rock Deformation: Laboratory Studies. Geophysical Monographs 36, pp. 263–288.
Schulmann, K., 1990. Fabric and kinematics study of the Bites orthogneiss (southwest Moravia): result of large-scale northeastward shearing parallel to the Moldanubian/Moravian boundary. Tectonophysics 177, 229–244.
Schulmann, K., Mlčoch, B., Melka, R., 1996. High-temperature microstructures and rheology of deformed granite, Erzgebirge, Bohemian Massif. Journal of Structural Geology 18, 719–733.
Schulmann, K., Lobkowicz, M., Melka, R., Fritz, H., 1995. Moravo-Silesian zone; Allochthonous units; structure. In: Dallmeyer, R.D., Franke, W., Weber, K. (Eds.), Pre-permian Geology of Central and Eastern Europe, pp. 530–540. IGCP 233 international conference, Goettingen.
Schulmann, K., Melka, R., Lobkowicz, M., Ledru, P., Lardeaux, J.M., Autran, A., 1994. Contrasting styles of deformation during progressive nappe stacking at the south-eastern margin of the Bohemian Massif (Thaya Dome). Journal of Structural Geology 16, 355–370.
Schwarzer, R.A., Hjelen, J., 2010. High-speed orientation microscopy with offline solving sequences of EBSD patterns. In: Klein, H., Schwarzer, R.A. (Eds.), Texture and Anisotropy of Polycrystals III. Trans Tech Publications, Switzerland, pp. 295–300.
Stipp, M., Kunze, K., 2008. Dynamic recrystallization near the brittle-plastic transition in naturally and experimentally deformed quartz aggregates. Tectonophysics 448, 77–97.
Stipp, M., Stünitz, H., Heilbronner, R., Schmid, S.M., 2002. The eastern Tonale fault zone: a 'natural laboratory' for crystal plastic deformation of quartz over a temperature range from 250 to 700 °C. Journal of Structural Geology 24, 1861–1884.
Štípská, P., Schulmann, K., 1995. Inverted metamorphic zonation in a basement-derived nappe sequence, eastern margin of the Bohemian Massif. Geological Journal 30, 385–413.
Štípská, P., Schulmann, K., Höck, V., 2000. Complex metamorphic zonation of the Thaya Dome; result of buckling and gravitational collapse of an imbricated nappe sequence. In: Cosgrove, J.W., Ameen, M.S. (Eds.), Forced Folds and Fractures. Geological Society Special Publication 169, pp. 197–211. London.
Suess, F.E., 1912. Die moravische fenster und ihre beziehung zum grundgebirge des hohen gesenkes. Akademie der Wissenschaften, Denkschrift Matematisch-Naturwissenschaftliche Klasse 88, 541–631.
Tullis, J., 1977. Preferred orientation of quartz produced by slip during plane strain. Tectonophysics 39, 87–102.
Turner, F.J., Weiss, L.E., 1963. Structural Analysis of Metamorphic Tectonites. McGraw-Hill Book Company, New York.
Ulrich, S., Schulmann, K., Casey, M., 2002. Microstructural evolution and rheological behaviour of marbles deformed at different crustal levels. Journal of Structural Geology 24, 979–995.
Ullemeyer, K., Braun, G., Dahms, M., Kruhl, J.H., Olesen, N.Ø., Siegesmund, S., 2000. Texture analysis of a muscovite-bearing quartzite: a comparison of some currently used techniques. Journal of Structural Geology 22, 1541–1557.
Vernooij, M.G.C., den Brok, B., Kunze, K., 2006. Development of crystallographic preferred orientations by nucleation and growth of new grains in experimentally deformed quartz single crystals. Tectonophysics 427, 35–53.
Wenk, H.R., Bunge, H.J., Jansen, E., Pannetier, J., 1986. Preferred orientation of plagioclase–neutron diffraction and U-stage data. Tectonophysics 126, 271–284.
Wenk, H.R., Kern, H., Schaefer, W., Will, G., 1984. Comparison of neutron and X-ray diffraction in texture analysis of deformed carbonate rocks. Journal of Structural Geology 6, 687–692.
Wilson, C.J.L., Russell-Head, D.S., Kunze, K., Viola, G., 2007. The analysis of quartz c-axis fabrics using a modified optical microscope. Journal of Microscopy 227, 30–41.
Wilson, C.J.L., Russell-Head, D.S., Sim, H.M., 2003. The application of an automated FA system to the textural evolution of folded ice layers in shear zones. Annals of Glaciology 37, 7–17.
Wilson, C.J.L., Robinson, J.A., Dugdale, A.L., 2009. Quartz vein fabrics coupled to elevated fluid pressures in the Stawell gold deposit, South-Eastern Australia. Mineral Deposita 44, 245–263.